Learning-assisted inversion for solving nonlinear inverse scattering problem

Kuiwen Xu, Zemin Qian, Yu Zhong, Jiangtao Su, Haijun Gao, and Wenjun Li

Abstract—Solving inverse scattering problems (ISPs) is challenging because of its intrinsic ill-posedness and the nonlinearity. When dealing with high nonlinear ISPs, i.e., those the scatterers with high contrast and/or electrically large size, the nonlinearity would be increased significantly. The traditional iterative nonlinear inversion methods converge slowly and take lots of computation time, even maybe trapped into local wrong solution. To alleviate the above challenges, a learning-assisted inversion approach termed as learning-assisted (LA) inversion method (LAIM) with advanced generative adversarial network (GAN) in virtue of a new recently established contraction integral equation for inversion (CIE-I) is proposed to solve the highly nonlinear ISPs with low computational cost. The preliminary profiles composed of only small amount of low-frequency components can be got efficiently by the Fourier bases expansion with CIE-I based inversion method (FBE-CIE-I). The physically exacted information can be taken as the input of the neural network to recover super-resolution image with more high-frequency components. A weighted loss function composed of the adversarial loss, mean absolute percentage error (MAPE) and structural similarity (SSIM) are used under pix2pix GAN framework. In addition, self-attention module is utilized at the end of generator network to capture the physical distance information between two pixels and enhance the inversion accuracy of the feature scatterers. In order to further improve the inversion efficiency, data-driven method (DDM) is used to achieve real-time imaging by cascading U-net and Pix2pix GAN, where U-net is used to replace FBE-CIE-I in LAIM. Compared with the other learning-assisted inversion, both synthetic and experimental examples have validated the merits of the proposed LAIM and DDM.

Index Terms—inverse scattering, highly nonlinear, pix2pix GAN, structural similarity (SSIM), self-attention, real-time imaging.

I. INTRODUCTION

ELECTROMAGNETIC inverse scattering problems (ISPs) aims to recover the location, geometric shape and constitutive parameters of unknown objects within a bounded domain of interest (DoI) through measured scattering field data. It has a wide range of applications in remote sensing [1], medical imaging [2]–[5], through-wall imaging [6], [7] and other fields [8]–[11]. The full-wave inversion aims to minimize

K. Xu and Z. Qian are with Engineering Research Center of Smart Microsensors and Microsystems, Ministry of Education, Hangzhou Dianzi University, Hangzhou China (e-mail: kuiwenxu@hdu.edu.cn).

Y. Zhong is FINIAC Pte. Ltd., Singapore (zhongyu@finiac.io).

J. Su, H. Gao and W. Li are with the Key Laboratory of RF Circuit and System, Ministry of Education, College of Electronics and Information, Hangzhou Dianzi University, Hangzhou 310018, China.

the mismatches between the synthetic data and the measured field data with model-based optimization.

However, owing to limited measurement data, it is well known that solving ISPs is difficulty and challenging due to the large number of unknowns, ill-posedness, and nonlinearity [12]. The nonlinearity with respect to the unknown constitutive parameters in the domain of interest (DoI) is due to multiple scattering effects inside the DoI.

The traditional model-based inversion methods are usually divided into two types, i.e., linear inversion and nonlinear iterative method. The linear inversion methods usually are based on the Born approximation (BA) [13], which can quickly reconstruct the physically constitutive information of the scatterers, but they are only suitable for the weak scatterers. For medium scatterers, nonlinear iterative inversion should be used, such as contrast source inversion method (CSI) [14], [15], subspace optimization method (SOM) [16], [17], distorted Born iteration method (DBIM) [18], and Newton-type methods [19]. In order to find the global minima extremes, some stochastic methods are also applied to solving the nonlinear ISPs [20]–[23], such as particle swarm optimization (PSO), covariance matrix adaptaion evolutionary strategy (CMA-ES), evolutionary programming (EP) and differential evolution algorithm (DEA). However, these methods come at the high computational resources. All of the above-mentioned methods, which are modeled by the Lippmann-Schwinger integral equation (LSIE), strongly depend on the initial guess to obtain the global solution and easily fall into the local solution, especially in the case of the strong scatterers with high contrast and/or electrically large size. For example, these methods could only reconstruct the test bench example of "Austria" profile with relative permittivity being smaller than 2.5. Therefore, for problems that cannot be successfully tackled by the traditional nonlinear inversion approaches based on LSIE, herein we refer to them as the highly nonlinear problems. With the increase of the relative permittivity of the "Austria" profile, the ISPs become highly nonlinear, as mentioned in [24]. For this kind of problems, different inversion models are needed, such as the one proposed in [25]–[27], where the maximum of the retrievable relative permittivity of "Austria" profile could be 4.5. However, the inversion usually takes three round optimizations with several hundreds or even more than 1000 iterations altogether, which takes much more computational cost than the medium nonlinear problems. Therefore, in order to tradeoff between the inversion capability and imaging efficiency, the inversion approach to efficiently solve the high nonlinear ISPs is significantly demanded.

Recently, machine learning is applied into the electro-

magnetic imaging to accelerate the inversion, [28]–[35]. The learning-based inversion methods can be generally divided into three types [28], [29]. The first one is d irectly retrieve the scatterers with the measured field d ata (i.e., black-box method), which need to fully learn the governing physics of the inversion. In [30], the measured scattered field is fed into the convolutional neural network (CNN) to recover physical information of the scatterer. The second one is follow the conventional iterative inversion to minimize the loss function, whereas replace some key operators (usually with the large amount of computations, i.e., gradient) with the neural networks to accelerate the inversion [31]. In [32], the inversion method is divided into three stages. Firstly, an initial guess of the contrast source can be obtained via some deterministic method. Then, a U-net network is used to obtain a better estimate of the contrast source with more high-frequency components. Finally, an iterative method such as SOM is used to achieve imaging by taking the obtained contrast source in the second step as the initialization. The third one is denoted as physics-inspired learning approach by incorporating domain knowledge and prior knowledge of physics into the networks, which typically decouples the full-wave inversion into a two-step reconstruction [33]–[35]. For example, a rough reconstruction by fast imaging methods like backpropagation (BP) can be obtained by the measured field data. Then a U-net network is employed to further enhance the quality of image [34], [35]. Besides, GAN is also used to improve the performance of the network by adversarial training in the electromagnetic forward computation and inverse problems [36], [37]. Although the existing learning-based inversion methods have achieved some success in terms of computational speed and imaging quality, they are suitable for solving the ISPs with moderate scatterers whereas still encounter large difficulty f or s olving h ighly n onlinear ISPs.

Inspired by the work in [38], to trade off the inversion ability for strong scatterers and the computational costs, a learning-assisted fast inversion approach by use of the new physical model, i.e., CIE-I, is utilized to solve the highly nonlinear ISPs. It decouples the full-wave inversion into a two-step reconstruction. Different from [38], the preliminary profile can be efficiently obtained by the Fourier bases expansion of CIE-I inversion (FBE-CIE-I) method with only a small number of low-frequency components [24]. Both fast convergence and strong capability could be kept via the FBE-CIE-I, then the super-resolution image with high-frequency components can be learned from the input preliminary image via advanced pix2pix GAN.

Herein, a weighted loss function composed of the adversarial loss, the mean absolute percentage error (MAPE) and structural similarity (SSIM) are used under the pix2pix GAN framework. In addition, self-attention module is utilized to further enhance the inversion accuracy of the unknown scatterers. With low-computational cost, the excellent performance of the proposed LAIM in term of inversion accuracy, generalization ability and stability can be achieved. As the first s tep i n the LAIM utilizes the iterative inversion, the efficiency c ould be restricted especially for three-dimensional (3D) ISPs. In order to further speed up the inversion procedure, a cascaded neural network is used to achieve real-time imaging, in which a data-driven method (DDM) with a U-net network replaces the FBE-CIE-I inversion method. However, the retrieved errors in the computation of the first step may propagate to the second step. Compared to the proposed LAIM, the inversion accuracy of the cascaded neural network named as DDM is slightly worse than the proposed single-network method named as LAIM. The contributions of the work can be summarized as follows:

1) A learning-assisted inversion approach under the CIE-I model is proposed to solve highly nonlinear ISPs. The proposed method achieves the tradeoff between the inversion ability for solving highly nonlinear ISPs and the computational cost. To some extent, the proposed LAIM method can achieve fast and accurate imaging for high contrast ISPs.

2) On the learning type method, the proposed PIM is established on physical model of CIE-I. The first step is to get the reconstruction profile via the Fourier bases expansion of CIE-I inversion (FBE-CIE-I) with proper regularized parameters after a small number of iterations. The physical information with low-frequency components can be well extracted by the first step with exactly low computation cost (e.g., less than 2 s). And the high-frequency components of the profile could be retrieved well almost in real-time by use of the proposed advanced GAN with redesigned loss function and self-attention module for the scatterers inside the domain of interest. The reasons behind these could be attributed to two fold1) The measured scattering field data could be transformed into the preliminary imaging of the relative permittivity by use of the powerful FBE-CIE-I with only small number of low-frequency components. The normalized physical dimension is achieved with small computation cost. 2) The image-to-image transformation is achieved via the advanced pix2pix GAN, in which the redesigned loss function is redesigned in terms of the network, the shape, and the quantitative value of the relative permittivity. Besides, self-attention module is used for the regularization of the physical equations and mimicking the multiple scattering effect in the modeling.

3) Compared to other methods based on the neural network, such as the data-driven method (DDM) directly with the input of the measured scattered fields for the U-net and the methods in [38], the numerical examples validate that the proposed method has better inversion accuracy, robustness, and the stability. Although DDM could almost achieve real-time imaging, it could only solve nonlinear ISPs with medium contrast. Whereas the LAIM could also work when dealing with highly nonlinear problems. The difference between the DDM and LAIM is the first step, in which the U-net is used to implement function of the FBE-CIE-I. Owing to that the data-driven U-net depends on the dataset supplied by FBE-CIE-I, the stability and inversion accuracy of DDM is not as good as the LAIM.
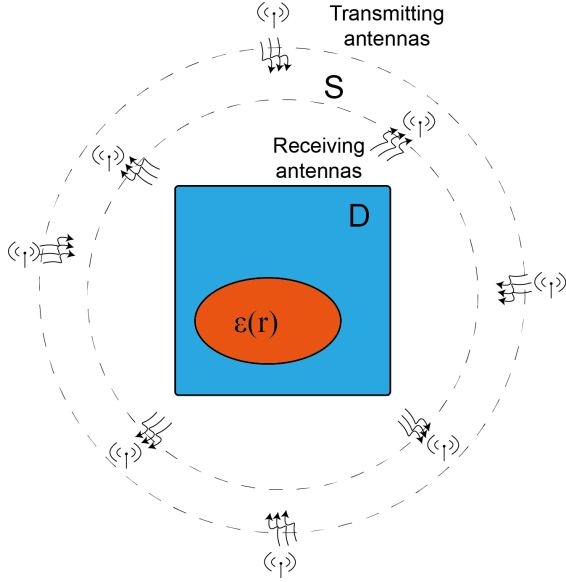
Fig. 1. Configuration of inverse scattering problems. The transmitting antennas illuminates the DoI D where a unknown scatterer is located, and the scattered field is collected by the receiving antennas. Here, the transmitting antennas and the receiving antennas are placed along a circular boundary S.

II. FORMULATION OF THE PROBLEM

In this paper, a two-dimensional (2-D) ISPs with transverse-magnetic (TM) polarization is considered and time-harmonic field is assumed with $e^{-i\omega t}$ (ω is the angular frequency). The 2-D configuration of ISPs is shown in Fig. 1. Unknown scatterers are located in the DoI D under a free-space homogeneous background which the permittivity, permeability and the wave number are ε_0, μ_0 and $k_0 = \omega\sqrt{\mu_0\varepsilon_0}$, respectively. In the measurement domain S, N_i transmitting antennas and N_r receiving antennas are placed uniformly along a circular line to collect the scattered fields. The transmitting antennas are located at r_p with $p = 1, 2, ..., N_i$ to illuminate the DoI in sequence, and the scattering field data is collected by the receiving antennas located at r_q with $q = 1, 2, ..., N_r$. The ISPs aim to reconstruct the constitutive parameters of the unknown targets given a set of $N_r \times N_i$ scattering data.

A. Forward Problem Modeling

In the forward problem, it is to get the scattered field from the known scatterers and given incident fields. In the following, the 2-D Lippmann-Schwinger integral equation (LSIE) is used to build the formulas. The total fields $E_p^t(\mathbf{r})$ in the DoI and the scattered field $E_p^s(\mathbf{r})$ on the measurement domain can be expressed by the following two equations,

$$E_p^t(\mathbf{r}) = E_p^i(\mathbf{r}) + k_0^2 \int_D G(\mathbf{r}, \mathbf{r}')I_p(\mathbf{r}')d\mathbf{r}', \mathbf{r} \in D \quad (1)$$

$$E_p^s(\mathbf{r}) = k_0^2 \int_D G(\mathbf{r}, \mathbf{r}')I_p(\mathbf{r}')d\mathbf{r}', \mathbf{r} \in S \quad (2)$$

where (1) and (2) are the field equation and the data equation. $E_p^t(\mathbf{r})$ and $E_p^i(\mathbf{r})$ denote the total electric field and incident field at $\mathbf{r}$ in the D by the pth incidence, respectively. $G(\mathbf{r}, \mathbf{r}')$ is the Green function for 2-D TM case in free space, i.e.,

$G(\mathbf{r}, \mathbf{r}') = \frac{i}{4}H_0^1(k_0|\mathbf{r} - \mathbf{r}'|)$, where $H_0^1(k_0|\mathbf{r} - \mathbf{r}'|)$ is the first-kind zeroth-order Hankel function.

The contrast source is defined as $I_p(\mathbf{r}) = \chi(\mathbf{r})E_p^t(\mathbf{r}), \mathbf{r} \in D$ with $\chi(\mathbf{r}) = \varepsilon_r(\mathbf{r}) - 1$, where ε_r is the permittivity of D. In [26], the contraction integral (CIE-I) is proposed to reduce the nonlinearity of the ISPs. Both sides of (1) are multiplied by the modified contrast function $R(\mathbf{r}) = \beta(\mathbf{r})\chi(\mathbf{r})[\beta(\mathbf{r})\chi(\mathbf{r})+1]^{-1}$. Then, we can get the contraction integral equation,

$$\beta(\mathbf{r})I_p(\mathbf{r}) = R(\mathbf{r})[\beta(\mathbf{r})I_p(\mathbf{r}) + E_p^i(\mathbf{r}) + \int_D G(\mathbf{r}, \mathbf{r}')I_p(\mathbf{r}')d\mathbf{r}'], \mathbf{r} \in D \quad (3)$$

$\beta(\mathbf{r})$ is a constant which has a positive real part and non-negative imaginary part.

Herein, the rectangular DoI is chosen to numerically implement the method of moments (MoM) with the pulse basis function and the delta testing function used to discretize the D into $M = M_1 \times M_2$ rectangle subunits. The numbers of subunits along the x- and y-axes are M_1 and M_2. The centers of subunits are located at $\mathbf{r_1}, \mathbf{r_2}, ..., \mathbf{r_M}$. When the subunits are small enough, the relative permittivity is equivalent to a constant in each subunit. For the pth incidence, the above equations can be written as discrete form,

$$\bar{\bar{\beta}}\bar{I}_p = diag(\bar{R}) \cdot [\bar{\bar{\beta}}\bar{I}_p + \bar{E}_p^i + \bar{\bar{G}}_D \cdot \bar{I}_p], \quad (4)$$

$$\bar{E}_p^s = \bar{\bar{G}}_S \cdot \bar{I}_p, \quad (5)$$

where $\bar{R} = \frac{\bar{\bar{\beta}}\bar{\chi}}{\bar{\bar{\beta}}\bar{\chi}+1}$, the Green's function $\bar{\bar{G}}_D$ maps the induced current to the scattered fields in the DoI, and $\bar{\bar{G}}_S$ represents the mapping between the induced current in the DoI and the scattered fields of the measurement domain S. (4) and (5) can be denoted as the object equation and data equation.

Here, we use H to denote the operator of forward modeling and the scattered field can be expressed as E_p^s by $E_p^s = H(\varepsilon_r, E_p^i)$. The inverse problem which retrieves the permittivity of the unknown scatterer can be regarded as an model-based optimization process,

$$\min : f(\varepsilon_r) = \sum_{p=1}^{N_i} \left\| H(\varepsilon_r, E_p^i) - E_p^s \right\|^2 + \lambda \Upsilon(\varepsilon_r) \quad (6)$$

where $\Upsilon(\varepsilon_r)$ is a regularization term, and λ is a weighting parameter to balance the data fitting term and the regularization term. In the nonlinear inversion methods, to alleviate the ill-posedness and serious nonlinearity, the cost function is composed of two terms, in which (4) is utilized as a regularization term to stabilize the data equation (5) [14].

B. FBE-CIE-I

In the twofold subspace optimization method (TSOM) [16], the induced current is divided into deterministic part of current (DPIC) and ambiguous part of current (APIC). DPIC can be obtained by the spectrum analysis of the operator $\bar{\bar{G}}_S$ in advance and APIC can be obtained via the two-step CG optimization. However, as the nonlinearity of ISPs increases, the proportion of DPIC appears to be very small, even negligible,

which has been verified in [32]. Herein, as discussed in [24], the Fourier bases-expansion on the induced current coupled with CIE-I (denoted as FBE-CIE-I) is used to extract the low-frequency components then these feature map are taken into the neural network. The role of neural network is to learn the high-frequency components according to the physically retrieved low-frequency components. Herein, the FBE-CIE-I will be introduced briefly as following [24].

In FBE-CIE-I, the induced current can be expanded by the discrete Fourier bases,

$$\bar{I}_p = vec\{\text{IDFT}(\bar{\bar{\gamma}}_p)\} \tag{7}$$

where $\bar{\bar{\gamma}}_p$ is 2D Fourier coefficients tensor, with the zero elements corresponding to the high-frequency Fourier components, the nonzero elements are corresponding to the low-frequency Fourier components. Tensor $\bar{\bar{\gamma}}_p$ contains four non-zero blocks of size M_F^2 in the four corners, where $M_0 = 4 \times M_F^2$. The inverse discrete Fourier transform (IDFT) is performed by the 2-D FFT algorithm and $vec\{\}$ denotes as the vectorization operator. For convenience, 2-D discrete inverse Fourier transform is denoted as F_T^*, mapping a sparse set of Fourier coefficients $\bar{\alpha}_p$ to the induced current subspace in C^2 space. The contrast source could be stated as in operator form

$$\bar{I}_p = F_T^*(\bar{\alpha}_p) \tag{8}$$

The residual of data equation (5) and object equation (4) of the CIE-I modeling can be defined as

$$\Delta_p^{\text{fie}} = \bar{E}_p^s - \bar{\bar{G}}_S \cdot F_T^*(\bar{\alpha}_p) \tag{9}$$

and

$$\Delta_p^{\text{cur}} = \bar{\bar{R}} \cdot (\bar{E}_p^i + \bar{\bar{G}}_D \cdot F_T^*(\bar{\alpha}_p)) - (\bar{\bar{\beta}} - \bar{\bar{R}} \cdot \bar{\bar{\beta}}) \cdot F_T^*(\bar{\alpha}_p) \tag{10}$$

Then, the cost function is defined as

$$f(\bar{\alpha}_1, \bar{\alpha}_2, \ldots, \bar{\alpha}_p, \bar{\bar{R}}) = \sum_{p=1}^{N_i}\{\frac{\|\Delta_p^{\text{fie}}\|^2}{\|\bar{E}_p^s\|^2} + \frac{\|\Delta_p^{\text{cur}}\|^2}{\|\bar{E}_p^i\|^2}\} \tag{11}$$

In the inversion, the CSI-type method is utilized to minimize the cost function (11) by alternately updating the contrast source and the modified contrast function via the conjugate gradient method and the least square method, respectively. Different from the inversion in [24], one round optimization would be implemented only and small number of Fourier bases are utilized for the expansion of the contrast source. Therefore, the number of unknowns (e..g, the contrast source) can be reduced significantly and the corresponding computation cost for the inversion can be lowered greatly.

The detailed procedure of the one-round FBE-CIE-I inversion method is summarized as follows:

1) n=0: Initialize the unknown parameters, $\bar{\bar{R}} = 0$, $\bar{\alpha}_{p,n} = 0$ with the dimensions of $M_0 \times 1$. According to the description in [24], a large value of β and a small number of low-frequency Fourier coefficients should be chosen.
2) Update $\bar{\alpha}_p$: $\bar{\alpha}_{p,n} = \bar{\alpha}_{p,n-1} + d_{p,n}\bar{v}_{p,n}$ where $d_{p,n}$ denotes the step length of the nth iteration and $\bar{v}_{p,n}$ denotes the conjugate gradient direction of the nth iteration.
3) Update the contrast source $\bar{I}_{p,n}$ and calculate the total field $\bar{E}_{p,n}^t$.

4) Update the modified contrast function $\bar{\bar{R}}_n$ by the least square method.
5) Update the contrast function: $\bar{\bar{\chi}}_n = \frac{\bar{\bar{R}}_n}{\bar{\bar{\beta}} - \bar{\bar{\beta}}\bar{\bar{R}}_n}$
6) Set the termination condition of iteration. If it is satisfied, the iteration would be stopped. Otherwise, set $n = n + 1$ and go to Step 2, and the termination conditions of the iteration are set as follows: $\delta^{2D} = \sqrt{\frac{1}{N_i}\left(\sum_{p=1}^{N_i}\frac{\|\bar{\alpha}_{p,n} - \bar{\alpha}_{p,n-1}\|^2}{\|\bar{\alpha}_{p,n-1}\|^2}\right)} < K$, where K is a constant, i.e., 0.02.

C. Proposed LAIM and DDM

Herein, a two-step learning inversion method (named as LAIM) based on the CIE-I are proposed to alleviate the challenge between the capability of high-nonlinear inversion problems and the large computational burden. The proposed LAIM is divided into the following two steps as depicted in Fig. 2,

1) The preliminary images with the low-frequency components are efficiently retrieved with the inversion method by the FBE-CIE-I.
2) The super-resolution imaging with large amount of the high-frequency components can be well got by the advanced pix2pix GAN.

However, to further improve the inversion efficiency, a U-net network is used to replace the FBE-CIE-I to speed up the first-step procedure and a cascaded neural network (named as DDM) is finally constructed to achieve the real-time imaging. The architecture of the proposed LAIM and DDM are shown in Fig. 2.
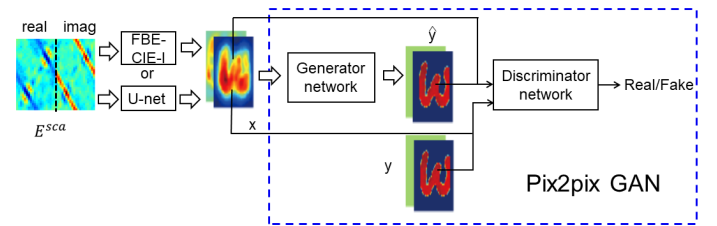

Fig. 2. Architecture of the proposed LAIM and DDM. The LAIM consists of two procedures, i.e., FBE-CIE-I and pix2pix GAN, and the DDM is composed of two cascaded network, i.e., U-net and pix2pix GAN.

III. NETWORK STRUCTURE

A. Pix2pix Generative Adversarial Network

The architecture of the pix2pix GAN model is shown in Fig. 3(a). As shown, the preliminary image which serves as the input of the self-attention assisted pix2pix GAN model is reconstructed by the FBE-CIE-I method in LAIM or a U-net network in DDM.

The pix2pix GAN model is divided into the generator network and the discriminator network. The generator network has a similar network structure as the U-net network which has a skip connection between contraction path and expansion path. The GAN mechanism is based on a two-player game.
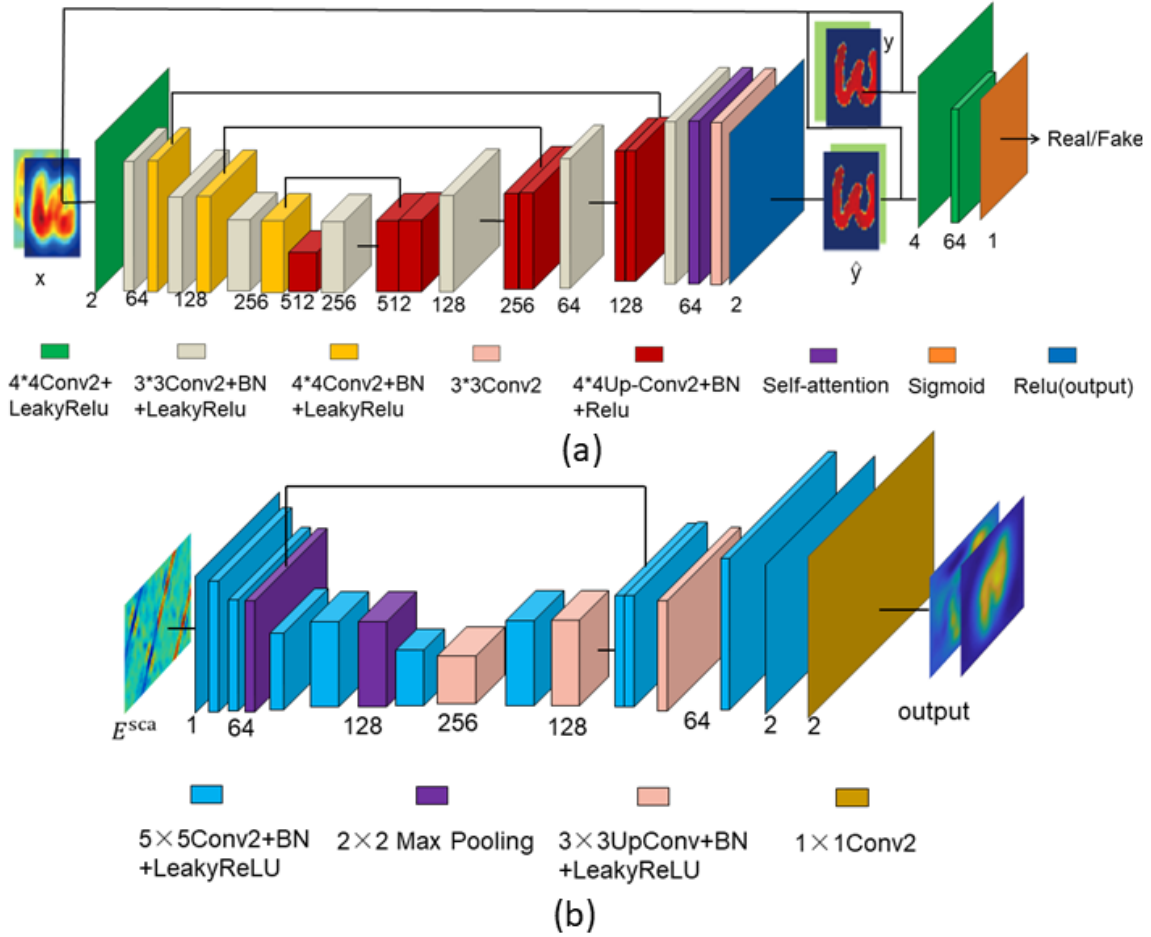
Fig. 3. (a) The pix2pix GAN architecture which is composed of discriminator network (D) and generator network (G) is used to reconstruct high resolution image. (b) The U-net architecture used in DDM.

The purpose of the generator network is to generate image which is similar to the target, while the purpose of the discriminator network is to identify the fake data generated by the generator network. The two restrict each other and eventually generate data so close to the target that the discriminator network can't recognize it. The real training dataset is taken as the input of the discriminator network together with these fake results. By doing so, the discriminator network will output a set of numbers between zero and one to determine whether the input image is real or fake.

In addition, a self-attention layer is added at the end of the generator network to improve the performance of the network. Due to the limitation of the size of the convolutional kernel, the traditional convolutional network can only capture the information association of the local area. However, self-attention obtains the corresponding weight (which is denoted as the global feature.) according to the relationship between any two pixels in the image.

In natural language processing (NLP), self-attention is used to capture the relationship between any two words in a sentence. Similarly in image processing, the main idea of self-attention module is to build an attention map containing the relationship between any two points. Attention map is used to extract features between any two pixels in the image,

such as the distance between two points. The input of self-attention layer obtains f(x), g(x) and h(x) through three 1×1 convolution layers. After transpose, f(x) is multiplied with g(x) and normalized to obtain attention map. The obtained attention map matrix contains the weight information between every two pixels. By updating convolution layer parameters during training process, attention map can learn the relationship between any two pixels. Then, we can get the output of the self-attention layer by multiplying h(x) and attention map. The details of the self-attention module can be seen in [39]. It is well known that the nonlinearity in inverse scattering depends on the multiple scattering effects of DoI, where the induced current at each pixel produces a scattered field at other pixel that depends on the distance between the two pixels. Therefore, self-attention could be used to capture the physical distance information between two pixels and better learn the multiple scattering process.

In conventional pix2pix GAN model, the loss function of the generator network is usually used as,

$$L_g = L_{\text{adv}} + \lambda \cdot L_1 \qquad (12)$$

where λ is the weight of the L_1, L_{adv} is adversarial loss which is designed to deceive the discriminator network. The

adversarial loss L_{adv} can be expressed as,

$$L_{\text{adv}} = \frac{1}{2}\|D(x,\hat{y}) - 1\|_2^2 \tag{13}$$

where $D(x,\hat{y})$ represents the output of the discriminator network when the inputs are x and $\hat{y}$. x and $\hat{y}$ denote the input and output of the generator network, respectively, and $\|\cdot\|_2$ denotes the L_2 norm. L_1 loss aims to make the reconstructed image being similar to the target image, which can be denoted as

$$L_1 = \frac{1}{M_1 * M_2}\sum_{i=1}^{M_1}\sum_{j=1}^{M_2}|\hat{y}_{i,j} - y_{i,j}|. \tag{14}$$

Herein, we replace L_1 in the loss function with the relative loss L_{MAPE} , which is defined as

$$L_{\text{MAPE}} = \frac{1}{M_1 * M_2}\sum_{i=1}^{M_1}\sum_{j=1}^{M_2}\left|\frac{\hat{y}_{i,j} - y_{i,j}}{y_{i,j}}\right|. \tag{15}$$

In addition, the SSIM index that measures the perceptual distance of two images considering the similarity of luminance, contrast and structure information, which could be formed as

$$\begin{aligned}L_{\text{SSIM}} &= 1 - \text{SSIM}(\hat{y}, y)\\ &= 1 - \frac{(2\mu_{\hat{y}}\mu_y + C_1)(2\sigma_{\hat{y}y} + C_2)}{(\mu_{\hat{y}}^2 + \mu_y^2 + C_1)(\sigma_{\hat{y}}^2 + \sigma_y^2 + C_2)}\end{aligned} \tag{16}$$

where $\mu_{\hat{y}}$ and μ_y denote the mean of $\hat{y}$ and y, $\sigma_{\hat{y}}$ and σ_y denote the standard deviation of $\hat{y}$ and y, $\sigma_{\hat{y}y}$ is the covariance of $\hat{y}$ and y. C_1 and C_2 are two constant parameters to avoid zero in the denominator. The mean and standard deviation reflect the luminance and contrast of the two images, respectively, while the covariance compares the structure information between them.

Although both L_{adv} and L_{SSIM} aim to generate images with similar features, the features they collected are different. The L_{adv} aims to generate images with similar features to the target image, which are collected by convolution kernel and contain some information such as edges and gradients. However, the L_{SSIM} measures the perceptual distance of two images by considering the similarity of luminance, contrast and structure information. Therefore, the pix2pix GAN and SSIM is combined together to make the generated image have more similar features with the target one. The modified loss function of the generator network is formulated as,

$$L_{\text{G}} = L_{\text{adv}} + \lambda_1 \cdot L_{\text{MAPE}} + \lambda_2 \cdot L_{\text{SSIM}} \tag{17}$$

where λ_1 and λ_2 are the weights of the L_{MAPE} and L_{SSIM}. And to better verify the validity of the proposed loss function, the numerical simulation with these two different loss functions, i.e., L_{G} and L_{g} are compared.

The loss function of discriminator network is denoted as

$$L_{\text{D}} = \frac{1}{2}\|D(x,\hat{y})\|_2^2 + \frac{1}{2}\|D(x,y) - 1\|_2^2 \tag{18}$$

Since generator network and discriminator network are optimized alternatively, the parameter tensor of one network is fixed when the other one is updated. The two neural networks would be trained in an adversarial way until reaching a Nash-equilibrium (namely a balance between the generator network and the discriminator network).

B. U-net Convolutional Neural Network

In DDM, the FBE-CIE-I is replaced with a U-net network to achieve the first step and the U-net network is cascaded with the pix2pix GAN to achieve real-time imaging. The input of the U-net network is the measured scattered fields. We extract the real and imaginary parts of the scattered field and concatenate them into a $N_r \times 2N_i$ real-value matrix, where the left and right part of the input are corresponding to the real and imaginary part of the scattered field, as depicted in Fig. 2. The target is the corresponding retrieved results by the FBE-CIE-I with the same hyperparameter setting in LAIM. The detail configuration of the U-net is depicted in Fig. 3(b) [40], [41]. It is composed of a contracting path and an expansive path. The contracting path follows a typical convolutional network structure, which consists of repeated convolutions, rectified linear unit (ReLU), batch normalization and several max pooling operations with a step of 2. Expansive path is similar to contracting path, but max pooling operation is replaced by up-convolution to up-sample the feature map. In addition, the size of the convolution kernels at the first two convolution layers of the contraction path is 5×5 to reduce the size of the feature map when the size of the other convolution kernels is 3×3.
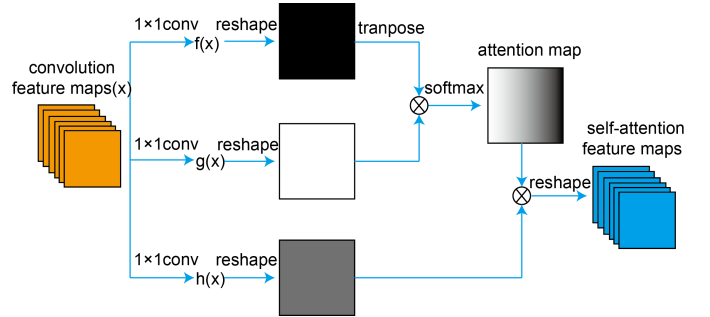

Fig. 4. Self-attention architecture. f(x), g(x), h(x) are the results of linear transformation and channel compression of the feature maps, $\otimes$ denotes matrix multiplication.

IV. NUMERICAL SIMULATION

In this section, several synthetic and experimental examples are used to verify the validity of the proposed methods in Section III. Firstly, we compare the performance of LAIM using the proposed loss L_{G} and self-attention module (denoted as 'self-attention pix2pix+L_{G}') with the one only using the conventional loss function L_{g} (denoted as 'pix2pix+L_{g}') and the one using both the conventional loss L_{g} and self-attention module (denoted as 'self-attention pix2pix+L_{g}'). Besides, some other typed learning-based inversion methods are also listed to validate the merits of the proposed LAIM, DDM and in the following.

A. Numerical Setup

In all of the numerical tests, the size of the DoI is $2 \times 2m^2$ and it is discretized into 64×64 pixels in the forward problem. The center of DoI is taken as the origin of the model. The number of transmitting and receiving antennas is 20 and 40 respectively, which are located uniformly over a circle S with radius of 3.75m. The operating frequency is set as 400 MHz. For each incidence, we calculate the scattered field using the MoM. The scattered field used in the training stage is always noiseless for all examples.

The handwritten digits in Mixed National Institute of Standards and Technology database (MNIST) are used as the training data for all synthetic examples. We randomly selected 8000 images from MNIST as the training data set, 1000 images as the validation data set and 1000 images for the testing data set. The relative permittivity is randomly distributed to [1, 3] with a minimum interval of 0.01 in the training set. In the training, to get the labels, the FBE-CIE-I is used to get the rough images with the the termination condition of K=0.02. M_F and β were set as 5 and 6, respectively. The average computational time cost is about two seconds in FBE-CIE-I. The hyperparameters in the neural network are set as follows: the learning rates of D and G are set as 0.0002, batchsize is set as 16 and the maximum number of iterative epochs in the training is set as 50. In the training, in order to balance the value of L_{adv}, L_{MAPE} and L_{SSIM} and keep the loss value almost in the same quantitative level, λ_1, λ_2 are set as 100 and 20. In addition, the samples used for neural network testing was added with 10% white Gaussian noise.

All network training and testing are operated on a server with Inter(R) Core(TM) i7-8700K CPU, 32G RAM, and GeForce RTX2080Ti GPU using PyTorch framework. In order to evaluate the image quality quantitatively, the error evaluation function is designed as follows:

$$R_{MAPE} = \frac{1}{M} \sum_{i=1}^{M_1} \sum_{j=1}^{M_2} \frac{\left| \varepsilon_{i,j} - \varepsilon_{i,j}^{true} \right|}{\left| \varepsilon_{i,j}^{true} \right|} \quad (19)$$

B. Numerical Tests

In the first example, MNIST and Letter data set with the relative permittivity between 1 and 3 were used to compare the inversion performance of the different inversions by the proposed LAIM. The reconstruction results of Test#1 to Test#4 are shown in Fig. 5. It can be observed that in the first step, the rough profile can be well got by the FBE-CIE-I, although the retrieval permittivity value is lower than the true value. With the good profile as the input of the network, all the three methods can obtain the pretty good reconstruction results.

Then, in order to test the generalization capabilities of the methods, several MNIST and Letter examples with the relative permittivity distributed between 3 and 3.5 were used to test in example 2. The corresponding reconstruction results are shown in Fig. 6. From the results in Fig. 5 and Fig. 6, by use of the attention mechanism, better reconstruction profiles can be obtained and the best retrieval results with
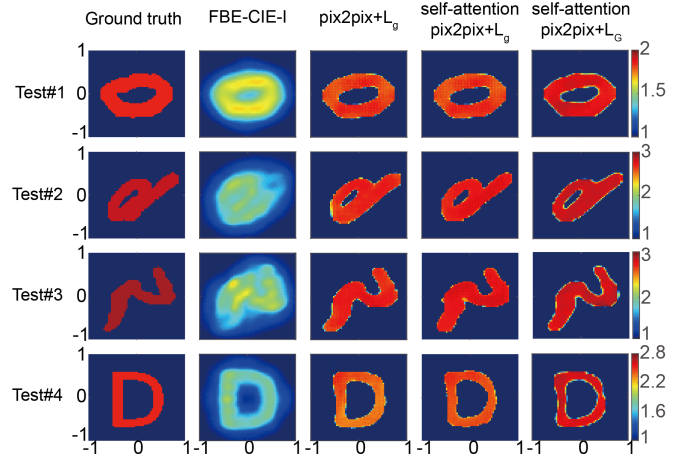

Fig. 5. Four representative examples with relative permittivity between 1 and 3. Test#1 to Test#3 are handwritten numerals "0", "9", "2" which are rotated. Test#4 is the letter "D".

TABLE I
Average error of the three methods in Example 1 and Example 2.

	Example 1	Example 2
pix2pix+L_g	3.24%	10.18%
self-attention pix2pix+L_g	2.99%	9.87%
self-attention pix2pix+L_G	2.66%	7.82%

more accurate relative permittivity can be achieved by 'self-attention pix2pix+L_G'. The average errors of the example 1 and example 2 are summarized in Table I. According to the reconstruction profiles and quantitative results, it is found that all the compared three methods can almost achieve imaging well in both two examples, while the reconstructed errors by use of the 'self-attention pix2pix+L_G' are slightly lower than others, which confirms the effectiveness of self-attention mechanism and the proposed weighted loss function.
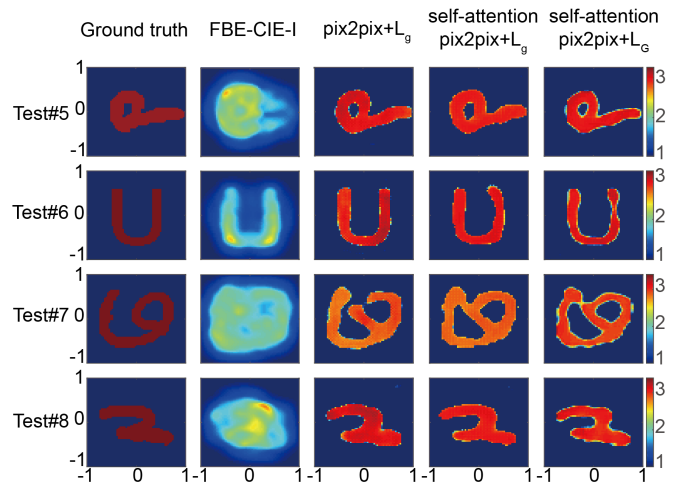

Fig. 6. Four representative examples with relative permittivity between 3 and 3.5 which is out of training set. Test#5, Test#7 and Test#8 are handwritten numerals "9", "6", "2" which are rotated. Test#6 is the letter "U".

In the third example, the benchmark testing profile, i.e., "Austria", which is much more challenging than the previously

TABLE II
The error of "Austria" test under different relative permittivity

	$\epsilon_r = 2$	$\epsilon_r = 3$	$\epsilon_r = 3.5$	$\epsilon_r = 3.7$
pix2pix+L_g	4.88%	17.0%	18.06%	26.17%
self-attention pix2pix+L_g	4.55%	14.9%	16.93%	24.58%
self-attention pix2pix+L_G	4.06%	9.56%	13.32%	16.57%

TABLE III
Average reconstruction time and errors of the proposed LAIM, DDM and MCSC

	LAIM	DDM	MCSC
Average computational time	2.28s	0.08s	0.15s
Average error	2.66%	5.07%	6.96%

mentioned examples, is used for testing. Here, the reconstructed results of "Austria" with relative permittivity of 2, 3, 3.5, 3.7 are depicted in Fig. 7, and the corresponding reconstruction errors, i.e., R_{MAPE}, of four tests are summarized in Table II. Through the comparison of visual imaging profiles and quantitative error, it is found that the proposed LAIM with 'self-attention pix2pix+L_G' exhibits better generalization ability and stability. And the retrieval highest relative permittivity can be up to 3.7, which exhibits the strong inversion ability against solving highly nonlinear ISPs. It is believe that the capability for solving high nonlinear ISPs will be further improved with more diversity training samples.
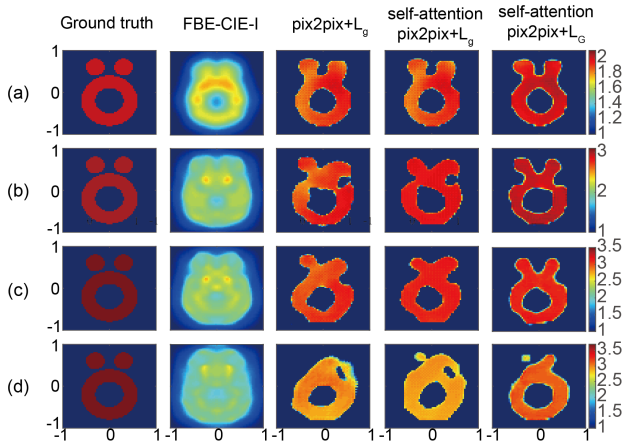
tional cost and reconstruction accuracy, the proposed DDM is used to achieve the almost real-time imaging while keep the better reconstruction performance than MCSC. Therefore, the proposed LAIM and DDM have their own merits compared to each other in terms of the inversion time and reconstruction accuracy.

To verify the performance of the proposed LAIM under different noise level, the test bench examples of "Austria" profile with the relative permittivity of 3.5 under 10%, 20% and 30% Gaussian noise level are tested, respectively. The corresponding reconstruction images are shown in Fig. 9. It can be seen that the proposed LAIM has good stability and robustness against noise.

Fig. 7. Reconstruction results for "Austria" profile with different relative permittivity. (a) $\epsilon_r = 2$, (b) $\epsilon_r = 3$, (c) $\epsilon_r = 3.5$, (d) $\epsilon_r = 3.7$.

Next, 'self-attention pix2pix+L_G' in frame of the pix2pix GAN is used for the comparison of the proposed LAIM and DDM. To highlight the merits of the proposed method, the modified contrast scheme by the contrast (MCSC) proposed in [38] is used for comparison under the same training data sets. MCSC method is also divided into two steps. In the first step, it uses SOM based on CIE model to obtain preliminary images by only two iterations. And in the second step, the U-net network is used to recover the high-resolution images.

Four representative tests are depicted in Fig. 8. To quantitatively compare the computational efficiency and accuracy of the above three methods, 100 examples are randomly selected from testing set for reconstruction to obtain the average computational time and average inversion error, which are listed in Table III. It can be easily found that the proposed LAIM has much better performance than both the DDM and the MCSC in term of the reconstruction accuracy. Whereas, among them, the computational cost of the proposed LAIM is much higher than DDM and MCSC. To tradeoff the computa-
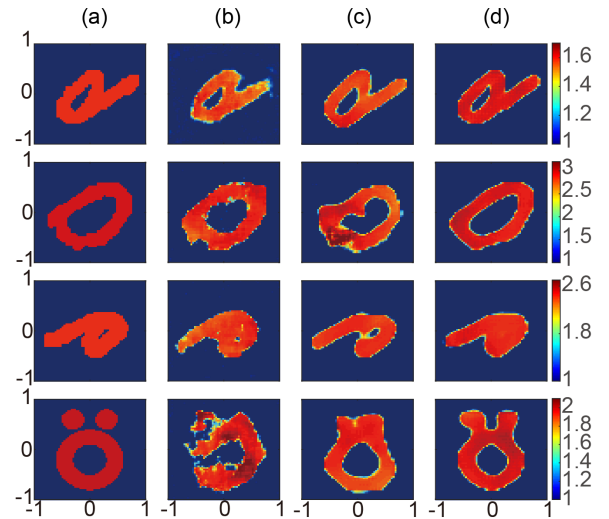

Fig. 8. (a) Ground Truth. Four representative tests with relative permittivity between 1 and 3 to compare the performance of (b) MCSC, (c) DDM and (d) LAIM.
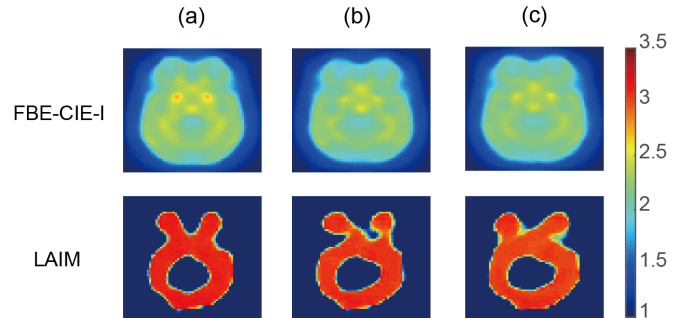

Fig. 9. Reconstruction results of "Austria" profiles with the relative permittivity of 3.5 under (a) 10%, (b) 20% and (c) 30% white Gaussian noises.

C. Experimental Tests

We also tested the *"FoamDielExt"* experimental data measured by the Institute Fresnel. As shown in the Fig .10(a), the *"FoamDielExt"* consists of a foam cylinder with the diameter of 80mm and a plastic cylinder with the diameter of 31mm in the DoI of 20cm × 20cm. The relative permittivity of the foam and plastic are 1.45 ± 0.15 and 3 ± 0.3, respectively. 8 transmitters and 241 receives are used to collect the scattered field at the frequencies from 2 to 10 GHz with a step of 1 GHz. The source-object centre and object centre-receiver distances are 1.67m. More details can be found in [42].
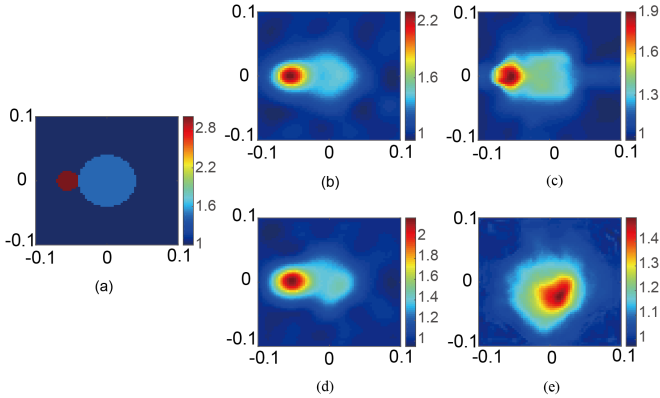

Fig. 10. Test on *"FoamDielExt"* profiles. (a) Ground Truth. Reconstruction results by FBE-CIE-I at (b) 3 GHz (c) 6 GHz. Reconstruction results of the first step in DDM at (d) 3 GHz (e) 6 GHz.
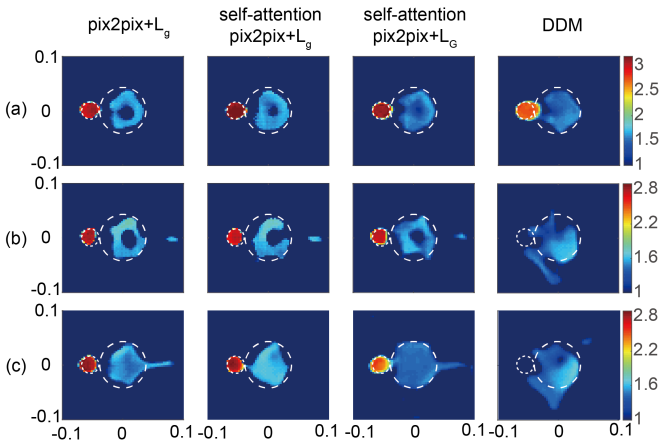

Fig. 11. Reconstruction results using 3 GHz training data set at (a) 3 GHz (b) 6 GHz. And (c) reconstruction results using 4 GHz training data set at 6 GHz.

In this example, we randomly add a circle on MNIST data set(denoted as "MNIST+Circle") to supply the more diversity of the samples in the training set and the relative permittivity of the profiles are set between 1.5 and 3.3. Fig. 10(b) and (c) represent the preliminary reconstruction results by the FBE-CIE-I at 3 GHz and 6 GHz and the good rough profiles with low-frequency components can be got. Fig. 10(d) and (e) depict the retrieval results of the U-net network in DDM. After carefully comparison in Fig. 10, although the reconstructed profiles at 3 GHz by both of two methods are kept in the same

TABLE IV
Reconstruction errors using 3 GHz data set by four methods at (a) 3 GHz (b) 6 GHz and Reconstruction errors using 4 GHz data set by four methods at (c) 6 GHz.

	(a)	(b)	(c)
pix2pix+L_g	3.44%	3.67%	2.98%
self-attention pix2pix+L_g	2.98%	3.59%	2.68%
self-attention pix2pix+L_{full}	2.52%	2.97%	2.21%
DDM	3.01%	4.84%	5.02%

level, the retrieved results at 6 GHz by U-net look deformed in which the position of the target is a litter misplaced. After the preliminary rough profiles, then they are used as the input of the pix2pix GAN to get the final reconstructed profiles with more high-frequency components. Firstly, the data set generated with the "MNIST+Circle" operating at 3 GHz is used to train the network, the final reconstructed results by 'pix2pix+L_g', 'self-attention pix2pix+L_g', 'self-attention pix2pix+L_G' and DDM are shown in Fig. 11(a) and (b). The quantitative errors are also listed in Table IV. It is concluded that LAIM with the 'self-attention pix2pix+L_G' achieves much better image quality in the experimental data compared to the other methods. It indicates that the proposed loss function and the attention mechanism under the frame of the pix2pix GAN works well when dealing with highly nonlinear ISPs. The proposed DDM can recover the image well at the 3 GHz, but it almost fails in restoring the profiles at the 6 GHz due to the distorted result in the first step.

Then, to verify whether improving the frequency of the training data set can help enhance the imaging quality, the data set at 4 GHz is used to train the network. The reconstruction results at 6 GHz are shown in Fig. 11(c). From both the reconstructed profiles and the quantitative results in Table IV, it is validated that the reconstructed methods using higher frequency, i.e., 4 GHz data set, have better performance than those with lower frequency (e.g., 3 GHz) data set. It is probably owing to that the more high-frequency components are incorporated into the training data sets at the higher frequency being closed to the test one. Through the experimental tests, it is found that we can achieve better imaging performance by reasonably improving the frequency of the training sets to solve the high-frequency ISPs to some extents.

In summary, the proposed method are tested on the three examples including the MNIST and Letter digits, the "Austria" profile and the Fresnel experimental data. All the results verify the effectiveness of the proposed weighted loss function and the self-attention mechanism to enhance the quality of reconstructions when dealing with highly nonlinear ISPs. In virtue of low-computation inversion of the FBE-CIE-I with only some amount of low-frequency components, LAIM can quickly recover the image well (about 2s). Also, to fulfill the real-time imaging, the DDM is also proposed to accelerate the inversion and could tradeoff the compromise between performance and speed.

D. Discussions on the inversion capability

According to the above results, highly nonlinear ISPs including both the imaging scatterers with higher contrast and electrically large size (operating on the higher frequency problems) have been intensively discussed via the numerical results from synthetic and experimental examples, respectively. The proposed LAIM could well reconstruct the highly nonlinear ISPs in almost real-time scenario, which has much faster speed and lower computational cost compared to the traditional iterative methods.

However, the generalization ability and stability to solve highly nonlinear ISPs is not as good as the conventional iterative methods [24]. For example, in the case of strong scatterers (i.e., Austria profile at 400 MHz), the proposed PIM can achieve the reconstruction well at the relative permittivity of 3.7, which is less than 4.5 in [24]. In our view, the disadvantage of the generalization ability is the an universal problems for the learning-based methods, which is owing to the limitation of the training set. A feasible way to improve the inversion capability is to adaptively change the range of the training data set according to the problem solved. So, if ISPs with higher contrast need to be solved, the training set with higher contrast should be also supplied accordingly, more high-frequency components and/or features should be extracted to characterize the more difficulty ISPs.

For example, owing to that the relative permittivity of the scatterers in the training set is ranged between 1 and 3, the maximum retrieval value is 3.7. If we set the range of relative permittivity as 3 to 4 (e.g., small range with higher contrast), the maximum reconstructed value could be larger than 4. The reconstructed profiles are depicted as Fig. 12. It can be seen clearly that ring and cylinder still have good reconstructed shapes and relative permittivity. It is known that, the test bench example Austria profile with the relative permittivity of 4.5 is a challenging case even by use of the conventional advanced methods based on CIE-I [27]. Although the top part of the reconstructed Austria looks a little deformed, the retrieved results is satisfied in terms of the entire shape and the relative permittivity. However, owing to physical limit of the FBE-CIE-I, if the features with small number of high-frequency components could not successfully exacted in the first step, then maybe the inversion on the more higher contrast of ISPs (e.g., Austria example) would be restricted. Therefore, the inversion capability of the proposed LAIM is limited by two main factors: 1) the physical model guiding in the network, and 2) the range of the training data set. We should tradeoff between the capability and the stability by use of the proposed method according to the application.

V. CONCLUSION

In this paper, a learning-assisted imaging approach named as LAIM by use of the pix2pix GAN are proposed to solve highly nonlinear ISPs. The rough image information composed of a few low-frequency components can be easily exacted by the FBE-CIE-I with quite low computational cost. Then the preliminary image can be taken as the input of the pix2pix GAN. The pix2pix architecture with self-attention in the generator network are used for inversion. In addition, a weighted
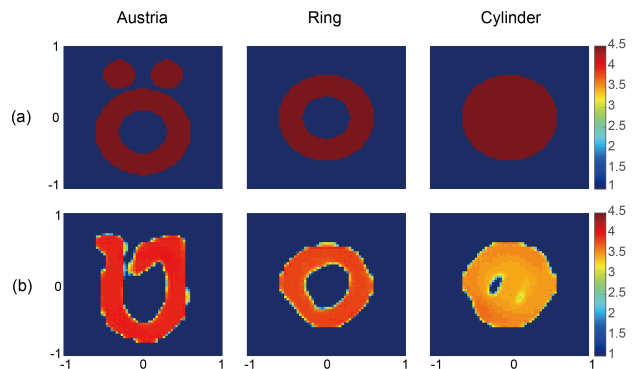

Fig. 12. Reconstructed profiles with $\epsilon_r = 4.5$ when the relative permittivity of the training set is between 3 and 4.

loss function which consists of the adversarial loss, MAPE and SSIM is utilized to effectively reduce artifacts of the reconstructions and thereby enhance the imaging quality. Good generalization capability and stability has also been validated by both numerical and experimental examples even for the challenging highly nonlinear cases. In addition, to tradeoff the compromise between the computational cost and the inversion accuracy, a U-net network is used to replace the iterative FBE-CIE-I and the DDM constructed by a cascaded neural network is used to fulfill the inversion in real time. Because the results obtained by U-net in the first step is inferior to the one by FBE-CIE-I, the reconstruction performance of DDM is slightly degraded, which maybe more suitable for the reconstruction of the moderate contrast scatterers. Consequently, the proposed LAIM can well reconstruct strong scatterers quickly, whereas the proposed DDM can achieve real-time imaging and its reconstruction accuracy is not as good as the LAIM. According to the different application scenarios, both of two proposed methods can show their respective merits well.

REFERENCES

[1] M. Datcu, K. Seidel, and M. Walessa, "Spatial information retrieval from remote-sensing images. I. Information theoretical perspective," *IEEE Trans. Geosci. Remote Sens.*, vol. 36, no. 5, pp. 1431-1445, 1998.

[2] L. Shen and R. Rangayyan, "A segmentation-based lossless image coding method for high-resolution medical image compression," *IEEE Trans. Med. Imag.*, vol. 16, no. 3, pp. 301-307, 1997.

[3] L. Xu and X. Wang, "Focused microwave breast hyperthermia monitored by thermoacoustic imaging: A computational feasibility study applying realistic breast phantoms," *IEEE J. Electromagn., RF, Microw. Med. Biol.*, vol. 4, no. 2, pp. 81-88, 2020.

[4] J. Li, B. Wang, D. Zhang, C. Li, Y. Zhu, Y. Zou, B. Chen, T. Wu, and X. Wang, "A preclinical system prototype for focused microwave breast hyperthermia guided by compressive thermoacoustic tomography," *IEEE Trans. Biomed. Eng.*, vol. 68, no. 7, pp. 2289-2300, 2021.

[5] X. Wang, T. Qin, R. S. Witte, and H. Xin, "Computational feasibility study of contrast-enhanced thermoacoustic imaging for breast cancer detection using realistic numerical breast phantoms," *IEEE Trans. Microw. Theory and Techn.*, vol. 63, no. 5, pp. 1489-1501, May 2015.

[6] F. Soldovieri, F. Ahmad, and R. Solimene, "Validation of microwave tomographic inverse scattering approach via through-the-wall experiments in semicontrolled conditions," *IEEE Geosci. Remote Sens. Lett.*, vol. 8, no. 1, pp. 123-127, 2011.

[7] R. Burkholder and K. Browne, "Coherence factor enhancement of through-wall radar images," *IEEE Antennas Wireless Propag. Lett.*, vol. 9, pp. 842-845, 2010.

[8] Y. Lin, J. Theiler, B. Wohlberg, Y. Wu, and Z. Zhang, "Data-driven methods for solving large-scale inverse problems with applications to subsurface imaging," *IEEE Southw. Symp. Image Anal. Interpret.*, pp. 13-13, 2020.

[9] K. Ozkan and N. Gencer, "Low-frequency magnetic subsurface imaging: Reconstructing conductivity images of biological tissues via magnetic measurements," *IEEE Trans. Med. Imag.*, vol. 28, no. 4, pp. 564-570, 2009.

[10] M. Benedetti, M. Donelli, D. Lesselier, and A. Massa, "A two-step inverse scattering procedure for the qualitative imaging of homogeneous cracks in known host media - preliminary results," *IEEE Antennas Wireless Propag. Lett.*, vol. 6, pp. 592-595, 2007.

[11] M. RodrIguez, M. Vera-Isasa, and V. Santalla, "3-D-Microwave breast tumor detection: Study of system performance," *IEEE Trans. Biomed. Eng.*, vol. 55, no. 12, pp. 2772-2777, 2008.

[12] X. Chen, "Computational methods for electromagnetic inverse scattering." Singapore: Wiley, 2018.

[13] G. Gao and C. Torres-Verdin, "High-order generalized extended Born approximation for electromagnetic scattering," *IEEE Trans. Antennas Propag.*, vol. 54, no. 4, pp. 1243-1256, 2006.

[14] L. Li, H. Zheng, and F. Li, "Two-dimensional contrast source inversion method with phaseless data: TM case," *IEEE Trans. Geosci. Remote Sens.*, vol. 47, no. 6, pp. 1719-1736, 2009.

[15] A. Zakaria and J. LoVetri, "Application of multiplicative regularization to the finite-element contrast source inversion method," *IEEE Trans. Antennas Propag.*, vol. 59, no. 9, pp. 3495-3498, 2011.

[16] K. Xu, Y. Zhong, R. Song, X. Chen, and L. Ran, "Multiplicative-regularized FFT twofold subspace-based optimization method for inverse scattering problems," *IEEE Trans. Geosci. Remote Sens.*, vol. 53, no. 2, pp. 841-850, 2015.

[17] X. Chen, "Subspace-based optimization method for solving inverse-scattering problems," *IEEE Trans. Geosci. Remote Sens.*, vol. 48, no. 1, pp. 42-49, 2010.

[18] Y. Wang and W. Chew, "An iterative solution of two-dimensional electromagnetic inverse scattering problem," *Int. J. Imaging Syst. Technol.*, vol. 1, pp. 100-108, 1989.

[19] P. Mojabi and J. LoVetri, "Overview and classification of some regularization techniques for the gauss-newton inversion method applied to inverse scattering problems," *IEEE Trans. Antennas Propag.*, vol. 57, no. 9, pp. 2658-2665, 2009.

[20] M. Donelli, G. Franceschini, A. Martini, and A. Massa, "An integrated multiscaling strategy based on a particle swarm algorithm for inverse scattering problems," *IEEE Trans. Geosci. Remote Sens.*, vol. 44, pp. 298-312, 2006.

[21] M. Hajebi, A. Hoorfar, E. Bou-Daher, and A. Tavakoli, "Inverse profiling of inhomogeneous subsurface targets with arbitrary cross sections using covariance matrix adaptation evolution strategy," *IEEE Geosci. Remote Sens. Lett.*, vol. 14, pp. 612-616, 2017.

[22] M. Hajebi, A. Tavakoli, and A. Hoorfar, "Frequency domain inverse profiling of buried dielectric ellipticalcylindrical objects using evolutionary programming," *IEEE Geosci. Remote Sens. Lett.*, vol. 15, pp. 503-507, 2018.

[23] C.-C. Chiu, C.-H. Sun, C.-L. Li, and C.-H. Huang, "Comparative study of some population-based optimization algorithms on inverse scattering of a two-dimensional perfectly conducting cylinder in dielectric slab medium," *IEEE Trans. Geosci. Remote Sens.*, vol. 51, pp. 2302-2315, 2012.

[24] K. Xu, L. Zhang, and Z. Wei, "Fourier bases-expansion contraction integral equation for inversion highly nonlinear inverse scattering problem," *IEEE Trans. Microw. Theory Techn.*, vol. 68, no. 6, pp. 2206-2214, 2020.

[25] M. DUrso, T. Isernia, and A. Morabito, "On the solution of 2-D inverse scattering problems via source-type integral equations," *IEEE Trans. Geosci. Remote Sens.*, vol. 48, no. 3, pp. 1186-1198, 2010.

[26] Y. Zhong, M. Lambert, D. Lesselier, and X. Chen, "A new integral equation method to solve highly nonlinear inverse scattering problems," *IEEE Trans. Antennas Propag.*, vol. 64, no. 5, pp. 1788-1799, 2016.

[27] K. Xu, Y. Zhong, and G. Wang, "A hybrid regularization technique for solving highly nonlinear inverse scattering problems," *IEEE Trans. Microw. Theory Techn.*, vol. 66, no. 1, pp. 11-21, 2018.

[28] A. Massa, D. Marcantonio, X. Chen, M. Li, and M. Salucci, "DNNs as applied to electromagnetics, antennas, and propagation - A review," *IEEE Antennas Wireless Propag. Lett.*, vol. 18, no. 11, pp. 2225-2229, 2019.

[29] X. Chen, Z. Wei, M. Li, and P. Rocca, "A review of deep learning approaches for inverse scattering problems (Invited Review)," *Prog. Electromagn. Res.*, vol. 167, pp. 67-81, 2020.

[30] S. Caorsi and P. Gamba, "Electromagnetic detection of dielectric cylinders by a neural network approach," *IEEE Trans. Geosci. Remote Sens.*, vol. 37, no. 2, pp. 820-827, March 1999.

[31] R. Guo, X. Song, M. Li, F. Yang, S. Xu, and A. Abubakar, "Supervised descent learning technique for 2-D microwave imaging," *IEEE Trans. Antenna Propag.*, vol. 67, no. 5, pp. 3550-3554, 2019.

[32] Y. Sanghvi, Y. Kalepu, and U. Khankhoje, "Embedding deep learning in inverse scattering problems," *IEEE Trans. Comput. Imaging*, vol. 6, pp. 46-56, 2020.

[33] L. Li, L. Wang, F. Teixeira, C. Liu, A. Nehorai, and T. Cui, "DeepNIS: Deep neural network for nonlinear electromagnetic inverse scattering," *IEEE Trans. Antenna Propag.*, vol. 67, no. 3, pp. 1819-1825, 2018.

[34] Z. Wei and X. Chen, "Deep-learning schemes for full-wave nonlinear inverse scattering problems," *IEEE Trans. Geosci. Remote Sens.*, vol. 57, no. 4, pp. 1849-1860, 2019.

[35] L. Zhang, K. Xu, R. Song, X. Ye, G. Wang, and X. Chen, "Learning-based quantitative microwave imaging with a hybrid input scheme," *IEEE Sens. J.*, vol. 20, no. 24, pp. 15007-15013, 2020.

[36] R. Song, Y. Huang, K. Xu, X. Ye, C. Li, and X. Chen, "Electromagnetic inverse scattering with perceptual generative adversarial networks," *IEEE Trans. Comput. Imaging*, vol. 7, pp. 689-699, 2021.

[37] Z. Ma, K. Xu, R. Song, C. -F. Wang, and X. Chen, "Learning-based fast electromagnetic scattering solver through generative adversarial network," *IEEE Trans. Antennas and Propag.*, vol. 69, no. 4, pp. 2194-2208, April 2021.

[38] Y. Zhou, Y. Zhong, Z. Wei, T. Yin, and X. Chen, "An improved deep learning scheme for solving 2-D and 3-D inverse scattering problems," *IEEE Trans. Antennas Propag.*, vol. 69, no. 5, pp. 2853-2863, 2021.

[39] X. Wang, Z. Cao, R. Wang, Z. Liu, and X. Zhu, "Improving human pose estimation with self-attention generative adversarial networks," *IEEE Access*, vol. 7, pp. 119668-119680, 2019.

[40] O. Ronneberger, P. Fischer, and T. Brox, "U-Net: Convolutional networks for biomedical image segmentation," *Proc. MICCAI*, pp. 234-241, 2015.

[41] K. Jin, M. McCann, E. Froustey, and M. Unser, "Deep convolutional neural network for inverse problems in imaging," *IEEE Trans. On Image Processing*, vol. 26, no. 9, pp. 4509-4522, 2017.

[42] G. Jean-Michel, S. Pierre, and E. Christelle, "Free space experimental scattering database continuation: Experimental set-up and measurement precision," *Inverse Probl.*, vol. 21, no. 7, pp. 117-130, 2005.